



Au nanorods-TiO₂ photonic crystal plasmonic-photonic hybrid sensor for label-free detection and identification of DNA molecules with single nucleotide polymorphisms

Daiki Kawasaki^a, Hirotaka Yamada^a, Kenji Sueyoshi^{a,b}, Hideaki Hisamoto^a, Tatsuro Endo^{a,*}

^a Department of Applied Chemistry, Graduate School of Engineering, Osaka Prefecture University, Sakai 599-8531, Japan

^b JST PRESTO, Japan Science Technology Agency, 4-1-8 Honcho, Kawaguchi, Saitama 332-0012, Japan

ARTICLE INFO

Keywords:

Plasmonics
Photonic crystal
Plasmonic-photonic hybrid
Plasmonic-photonic coupling
Label-free sensor
DNA analysis

ABSTRACT

Highly sensitive optical sensors for label-free detection of DNA must have high usability and wide applicability for achieving advances in the medical and biological science fields. However, current sensors do not simultaneously satisfy these criteria. Here, we developed a simple, cost-effective, and sensitive plasmonic-photonic hybrid sensor using gold nanorods as nanoantennae and a photonic crystal slab (PCS) as a microcavity. In this report, we performed simple microscopic detection and identification of DNA molecules with Alzheimer's disease-associated single nucleotide polymorphisms, which is an important indicator for early diagnosis. The PCS was fabricated using nanoimprint lithography; the gold nanorods were controllably coupled with the PCS. The device sensitivity was experimentally assessed by controlling the plasmonic-photonic coupling resonance, which was enabled by tuning the PCS-coupled AuNR amounts. The sensitivity was also investigated by theoretical modeling of the hybrid sensor, based on the temporal coupled mode theory (TCMT). The TCMT-based theoretical model well explained the experimental results. In a demonstration of ultrasensitive detection of DNA, the identification of single nucleotide mismatched DNA molecules (~ 1 pM) and detection of several DNA molecules (~ 1000), with a limit of detection of 5.9 aM, were successfully achieved. This sensor may thus have wide applications for DNA analysis.

1. Introduction

Label-free biomolecular analysis is fundamentally important to biological and medical sciences. Therefore, the development of techniques for label-free and highly sensitive biomolecule detection and identification will facilitate advances in the fields of biological and medical science [1–3]. Electrochemical methods such as field-effect transistors and nanopores have been applied for highly sensitive detection of biomarkers, such as proteins, DNAs, and RNAs [4–7]. Electrochemical sensors can fundamentally achieve high sensitivity owing to the electronic signal transportation that they permit; however, they intrinsically suffer from complicated electrical circuits, low multiplicity, and poor spatiotemporal resolution limits (in the order of ms). Optical techniques have also played important roles in bioanalysis [8–11]. Optical sensors can be used to realize high-spatiotemporal resolutions and simple operation systems with high sensitivity owing to photonic signal transportation.

Nanoantennae offer ultrasensitive nanospace based on an enhanced near-field generated by localized surface plasmon (LSP) [12–14]. Many metal nanostructures used as nanoantenna-based optical sensors for label-free detection of biomolecules have been reported; [15–18] however, the intrinsic losses that occur in metals (i.e., those resulting from a low quality factor (Q)) have limited the sensitivity and signal-to-noise ratio (SNR) of such devices [19,20]. Recently, considering the use of photonic crystals (PhCs) as optical microcavities with high Q -factors, PhC-coupled nanoantenna-based optical sensors have been investigated as plasmonic-photonic hybrid sensors [21–23]. These hybrid sensors have demonstrated their potential in highly sensitive, high-spatiotemporal, and label-free detection and analysis of biomolecules. However, the optical circuits and measuring systems of these devices are complex, and the use of such hybrid devices as optical sensing platforms requires complicated and expensive fabrication methods. These barriers, in terms of operability and accessibility, have prevented high-throughput and cost-effective fabrication of current

* Corresponding author.

E-mail address: endo@chem.osakafu-u.ac.jp (T. Endo).

<https://doi.org/10.1016/j.snb.2022.131747>

Received 13 January 2022; Received in revised form 1 March 2022; Accepted 17 March 2022

Available online 19 March 2022

0925-4005/© 2022 Elsevier B.V. All rights reserved.

hybrid sensors. Moreover, experimental investigation of the performance of such sensors is difficult, considering plasmonic–photonic interactions [22–25]. Because hybrid sensors are good candidates for use as next-generation optical sensors, their detailed characteristics should be explored. Recently, Liu et al. reported the first theoretical and experimental investigation of a plasmonic–photonic coupling regime using a gold nanorod (AuNR)- and titanium dioxide (TiO₂)-based PhC guide [26]. However, the relationship between the coupling regime and label-free sensing properties of such a system has not yet been revealed. Therefore, a high-throughput fabrication method is essential for detailed investigation of hybrid sensors, and the development of a simple and cost-effective method with high usability and wide applicability is crucial for advancement in biomedical sciences.

In this study, we generated a simple, cost-effective, and ultrasensitive optical sensor with a plasmonic–photonic hybrid structure that can be produced via a high-throughput fabrication process. We demonstrated highly sensitive detection and identification of DNA molecules with single nucleotide polymorphisms related to Alzheimer's disease, a condition that requires early diagnosis for improving the quality of life of the afflicted patients [27–30]. Our hybrid sensor was constructed using AuNRs and a TiO₂-based PhC slab (PCS). The PCS was fabricated using nanoimprint lithography, which allowed a high-throughput and cost-effective technique for PCS fabrication [31]. Moreover, the AuNRs were controllably coupled with the PCS, which helped to elucidate the correlation between the sensitivity and plasmonic–photonic coupling modes. To theoretically evaluate our hybrid sensor as a plasmonic–photonic hybrid system, a theoretical model of our hybrid sensor was also constructed based on the temporal coupled mode theory (TCMT) [26,32–34], and the finite-difference time-domain (FDTD) calculation method was used to assess this model [35]. Next, considering that the absorption losses attributed to the AuNRs would increase owing to DNA molecules attaching on the AuNR surface, the theoretical factor for the sensitivity of our hybrid sensor was derived from our TCMT-based hybrid model [36–39]. This hybrid system was then investigated for its ability to detect and identify DNA molecules using a simple microscopic method. Our hybrid sensor successfully identified DNA (1 pM) with a single mismatched base pair and detected several complementary DNA molecules. Moreover, a much lower limit of detection (LOD) of 5.9 aM (~1000 molecules) was achieved using the designed system [40–42].

2. Material and methods

2.1. Fabrication of the PCS and hybrid structure

The TiO₂-based PCS was fabricated via liquid phase deposition (LPD) and nanoimprint lithography [31]. A cycloolefin polymer (COP)-based nano-pillar array structure film, which was used as a mold, was washed with ethanol and ultrapure water. The surface was then modified by atmospheric plasma treatment. The COP mold was subsequently filled with an LPD solution (diammonium hexafluorotitanate (0.15 M, (NH₄)₂TiF₆), boric acid (0.45 M, H₃BO₃), and hydrochloric acid to adjust the pH to approximately 3.0) at 40 °C for 90 min. The TiO₂-deposited mold was then washed with water. After TiO₂ deposition, the TiO₂ layer was attached to the glass substrate using a photo-curable resin, followed by dissolution of the COP mold with D-limonene. The PCS was thereby obtained (Fig. S1). The COP mold (FLP230/200-120; pillar diameter and distance: 230 nm; height: 200 nm) was purchased from Scivax Co., Ltd. (Kanagawa, Japan). Diammonium hexafluorotitanate, ethanol, boric acid, and D-limonene were purchased from the Fujifilm Wako Pure Chemical Corporation (Osaka, Japan). The photo-curable polymer (NOA81) was purchased from Norland Products Inc. (Cranbury, USA). The hybrid structure was fabricated by incubating the PCS in an aqueous solution of dispersed AuNRs (~50 ng/ml, 200 µl) with or without the irradiation of white light using a homemade microscope for 60 min. The structure was then washed with ultrapure water to remove the AuNRs

that were weakly attached to the PCS surface. The aqueous solution of dispersed AuNRs was purchased from Sigma-Aldrich (Tokyo, Japan).

2.2. Fabrication of the hybrid sensor

First, probe DNA-functionalized AuNRs were prepared. To achieve this, a 5' disulfide-modified 23-base pair (bp)-long DNA sequence (referred to as probe DNA) was loaded onto the AuNR surface using the salt-aging method [43]. The oligonucleotides used in the present study are shown in Table S1 and were purchased from BEX Co., Ltd. (Toyota, Japan). To prepare the probe DNA-functionalized AuNRs, the aqueous solution of dispersed AuNRs (1 ml) was first centrifuged (3000 g, 30 min), and the supernatant was removed. Next, 500 µl of 2 µM probe DNA containing 0.1 M of phosphate buffer (PB) were added to the AuNR precipitate, and the solution was then sonicated for 10 s followed by incubation at 37 °C for 20 min. The concentration of NaCl was increased to 0.2 M by adding 100 µl of 2 M NaCl and 0.1 M phosphate-buffered saline (PBS) solution (pH 7.4). This solution was sonicated for 10 s and incubated at 37 °C for 20 min. This procedure was repeated until the concentrations of probe DNA and NaCl reached 1 µM and 1 M, respectively. The absorption spectra of the AuNR-dispersed PBS solutions with and without probe DNA were measured to confirm the immobilization of the DNA on the AuNR surface ($N = 3$). The PB and PBS solutions contained 0.1 mM EDTA, NaCl, Na₂HPO₄·12H₂O, and EDTA, which were used for preparing the buffer solutions, were all purchased from Wako Pure Chem. Co. (Osaka, Japan). Next, the hybrid sensor was fabricated using almost the same procedure used to fabricate the hybrid structure described above. The PCS was incubated in the probe DNA functionalized AuNR-dispersed solution, which was prepared as described above, for various times ($T = 30, 45, 60, 90$, or 120 min) with white light irradiation using the aforementioned homemade microscope. After washing with ultrapure water, the hybrid sensor was obtained.

2.3. Microscopy

The various structures were observed via field-emission SEM (SU8010, Hitachi, Ibaraki, Japan) at an acceleration voltage of 10 keV. Before these observations, Pt was sputtered onto the surface of each structure with a thickness of approximately 3 nm for a clearer observation of the obtained surfaces using SEM. The AuNR density was defined as the number of AuNR molecules inside (AuNR(in)) or outside (AuNR(out)) of the holes per 1 µm² of the PCS surface. The AuNR density was determined using the mean value obtained by observing five areas on a single hybrid structure chip (Fig. S2).

2.4. Optical measurements

An optical setup for reflectometry was constructed based on an upright microscope (Wraymer Inc., Osaka, Japan), which was composed of a tungsten-halogen lamp, lens, aperture, half-mirror, long-working-distance lens (Sigma Koki Co., Ltd., Hidaka, Japan), spectrometer, and operation software (Thorlabs Inc., Newton, USA). The reflection spectra of the structures were measured under ambient conditions, and the quality factors Q of the two spectral peaks (A and B) were calculated as $Q = \text{FWHM}/\lambda_{\text{peak}}$, in which FWHM is the full width at a half maximum that was obtained via spectral peak fitting according to the Lorentz function and λ_{peak} is the peak wavelength. The reflection intensity was normalized by that of the PCS in all measurements. The variation in the reflection intensity ΔR was calculated based on the normalized reflection intensity R .

2.5. Electromagnetic field calculations

The FDTD method was used for the electromagnetic calculations conducted in the present study. The commercially available calculation software (FDTD-solution, Ansys, Inc., Vancouver, Canada) was used.

The calculated structural model was constructed based on the fabricated structure. The diameter (d) and lattice constant (a) of the PCS were 200 and 460 nm, respectively. The diameter (D) and long-axis length (L) of AuNR were 30 and 65 nm, respectively. The mesh size was 2.5 nm^3 . AuNR(in) particles were located at the center of the holes, and AuNR(out) particles were located on top of the PCS surface, as shown in Fig. 1. The AuNR density was controlled by tuning the x-y periodic structure area such that the periodicity of the photonic crystal was not affected. The orientation of the AuNRs was fixed such that the long-axis was parallel to the x-direction. The boundary condition was “Periodic” along x-y direction and perfect matched layer (“PML”) along z-axis direction. According to the nonpolarized incident light in the experimental optical setup, the incident white light in the simulation was cross-polarized planewave of which wavelength range was from 400 to 900 nm. The reflection spectrum of the structure was then calculated, and the enhanced near-field ($|E|^2$) at the peak wavelengths λ_{peak} of peaks A and B was calculated, and its distribution was obtained. The calculated reflection spectrum was then analyzed as described above in the experimental method with respect to the Q -factor and normalized reflection intensity R . The average near-field intensities on the surfaces of AuNR(in) and AuNR(out) at peaks A and B were calculated, and the sum of the intensities at peaks A and B was defined as $\langle |E_{\text{in}}|^2 \rangle$ for AuNR(in) and $\langle |E_{\text{out}}|^2 \rangle$ for AuNR(out), respectively. The sum of the near-field intensities of AuNR(in) and AuNR(out) was defined as $\langle |E|^2 \rangle = \langle |E_{\text{in}}|^2 \rangle + \langle |E_{\text{out}}|^2 \rangle$, which describes the enhanced near-field intensity of the hybrid structure.

2.6. Detection and identification of DNA molecules

Complementary (Comp)-DNA, 1-base mismatched (1-mis)-DNA, and mismatched (mis)-DNA, purchased from BEX Co. Ltd. (Tokyo, Japan), were used as target DNA molecules in this study [27,28]. To investigate the use of the developed system for identifying DNA molecules, sample solutions (1 pM in a PBS buffer) of each of the three aforementioned types of DNA were prepared. The hybrid sensor was incubated in the DNA sample solution (250 μl) for 60 min at 37°C to hybridize the DNA molecules with the probe DNA that was immobilized on the AuNR surface. The samples were then washed with ultrapure water to remove the non-specifically adsorbed DNA molecules. The change in reflection intensity before and after incubation, ΔR_{det} , was calculated for the purpose of DNA identification. The sensitivity S was defined as

$S = \Delta R_{\text{det}} / \Delta R_{\text{load}}$ (ΔR_{load} is the change in reflection intensity before and after AuNR loading on the PCS), which describes the responsivity per unit of AuNR. To investigate the highly sensitive DNA detection of the developed system, comp-DNA sample solutions (1 aM to 100 fM in a PBS buffer) were prepared. Comp-DNA was hybridized using the procedure described above, and the calibration line relating the sensitivity S to the concentration of comp-DNA was obtained. Triplicate measurements for all DNA samples were conducted ($N = 3$).

3. Results and discussion

3.1. Plasmonic-photonic hybrid structure

The proposed hybrid sensor was fabricated using a simple, cost-effective, and high-throughput process. First, the TiO_2 -based PCS was fabricated using a nanoimprint technique (Fig. S1). This first phase of this fabrication process enabled the hybrid structure to be simply and rapidly produced on a large scale. Next, AuNRs were attached onto the PCS surface by immersion of the PCS into an aqueous solution of dispersed AuNRs ($< 50 \text{ ng/ml}$) with or without white light irradiation under a microscope for 60 min. Upon white light irradiation during the immersion, the AuNRs were attached inside and outside of the holes; conversely, in the absence of white light irradiation, the AuNRs were barely attached in the holes (Fig. S2). According to our previous study [31], it was expected that the confined light in the PCS holes generated by the photonic mode would attract AuNRs into the hole via the electric field gradient created under white light irradiation during the immersion process [44]. Moreover, our previous study suggested that the plasmonic mode of the AuNRs that attached inside of the holes would be efficiently coupled with the photonic mode of the PCS. Therefore, in this study, we mainly investigated the hybrid structure that was obtained using this immersion procedure with white light irradiation. Scanning electron microscopy (SEM) images of the hybrid structure are shown in Fig. 1A. The AuNRs attached inside of the holes are defined as AuNR(in), whereas those attached outside of the holes are defined as AuNR(out). The densities of the AuNR(in) and AuNR(out), which are defined by the number of AuNRs in a $1\text{-}\mu\text{m}^2$ area, were both approximately $0.55 \text{ counts}/\mu\text{m}^2$. The diameter of the AuNRs (D) was 30 nm, and the length (L) was 70 nm, while the diameter and lattice constant of the PCS were 200 and 460 nm, respectively (Figs. 1A and S3). The reflection spectrum was obtained using the reflectometric method with a homemade optical microscope, as shown in Fig. 1B. Based on the obtained hybrid structure and experimental optical system, the theoretical structure and optical

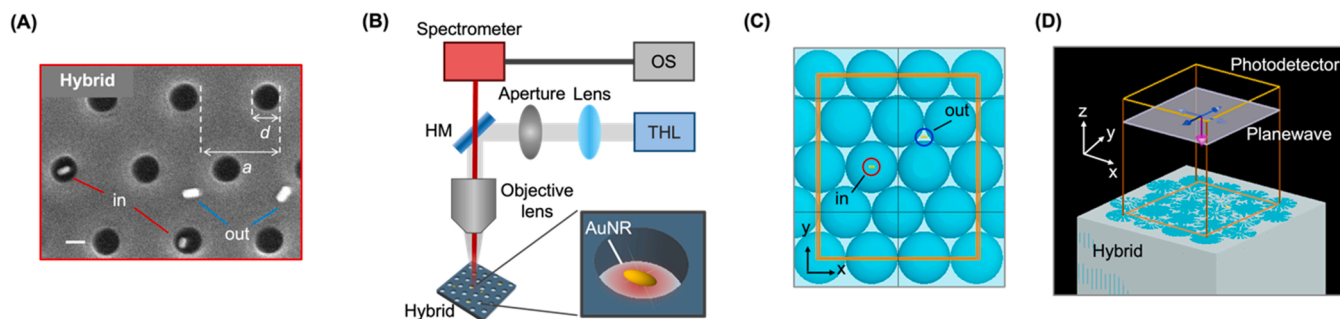


Fig. 1. Plasmonic-photonic hybrid structure. (A) SEM image of the plasmonic-photonic hybrid structure composed of PCS and AuNRs. AuNRs inside the holes were denoted as AuNR(in), and AuNRs outside the holes were denoted as AuNR(out). The density of each quantity was approximately $0.55 \text{ counts}/\mu\text{m}^2$. The diameter of the hole (d) was 200 nm, and the lattice constant (a) was 460 nm. The size of the AuNRs was $30 \times 70 \text{ nm} \pm 10\%$. The scale bar indicates 100 nm. (B) Illustration of a microscope-based homemade optical setup for reflectometry of the hybrid structure. HM indicates the half mirror, OS is the operation software for the spectrometer, and THL is the tungsten-halogen lamp. A long-working distance objective lens ($\times 10$) was used. No polarized incidental light was irradiated into the hybrid structure; the reflected light was corrected into the objective lens, and the reflection spectrum was obtained with a computer. (C) Surface of the simulation model of the hybrid structure. AuNR(in) is indicated with a red circle and AuNR(out) is indicated with a blue circle. The densities of AuNR(in) and AuNR(out) were $0.45 \text{ counts}/\mu\text{m}^2$. The diameter and lattice constant of the PCS and the AuNR size were set to be the same as the fabricated structure. (D) Schematic illustration of the optical setup for the reflectometry of the simulated hybrid structure. Based on the experimental setup, a cross-polarized planewave was irradiated into the hybrid, and the reflected light was measured using the intensity monitor as a photodetector.

measurement model for this system were constructed, and the reflection spectrum and electromagnetic field were subsequently calculated using the FDTD method (Fig. 1C and D). In the simulations, the densities of AuNR(in) and AuNR(out) were $0.45 \text{ counts}/\mu\text{m}^2$. The detailed simulation conditions are described in the Materials and Methods section. The absorption spectrum of the AuNRs dispersed in the aqueous solution and the reflection spectrum of the bare PCS are shown in Fig. S4. The experimental and simulated reflection spectra of the PCS and hybrid structure are shown in Fig. 2A and B, respectively. In addition, the reflection spectrum of the hybrid structure without AuNR(in), which was fabricated using the aforementioned procedure without light irradiation during immersion, is shown in Fig. S5. The wavelengths (λ_{peak}) and Q -factors ($Q = \lambda_{\text{peak}}/\text{FWHM}$) of the peaks from the experimental and simulated spectra were calculated, in which FWHM is the full width at half maximum. The spectra were fitted using Lorentzian curves. At peak A (Fig. S4), the λ_{peak} and Q -factor (Q_{PCS}) values were 640.5 nm and 137.6 in the experiment, respectively, and 633.6 nm and 141.8 in the simulation, respectively, which was denoted as mode A. At peak B, λ_{peak} and Q_{PCS} were 662.4 nm and 398.6 in the experiment, respectively, and 670.6 nm and 429.4 in the simulation, respectively, which was denoted as mode B (Fig. 2A and B). It was posited that the differences between the peak wavelengths and Q -factors of the experimental and simulated spectra may result from the structural and incidental angle differences between the experimental and simulated models. After AuNR loading, the peak intensity and Q -factor (Q_{Hyb}) both decreased without any peak shift in both the experiment and simulation. Conversely, in the case of the hybrid structure without AuNR(in) that is shown in Fig. S5, the reflection intensity at peak A did not change, whereas that at peak B slightly decreased. Fig. 2C shows the normalized electric fields ($|E/E_{\text{max}}|^2$, where E_{max} was maximum intensity of each structure) of the PCS and hybrid structural cross-section (x - z) around AuNR(in) at peaks A and B. The calculated electric fields around AuNR(out) are shown in Fig. S6A. At peak A, the light in the holes of PCS is dominantly confined within AuNR(in). Conversely, at peak B, the light on the slabs of PCS is confined within both AuNR(in) and AuNR(out). This phenomenon of light localization within AuNRs is expected to result from plasmonic–photonic coupling due to the overlapping of these resonance wavelengths, rather than the light confinement provided by the cavity to the nanoantennae, which has been observed when no spectrum overlap between the two optical elements occurs^{22, 23}. The decrease in the peak intensity is expected to result from the dissipative losses added to the

cavity by the nanoantennae in the coupling mode. The maximum field intensity $|E_{\text{max}}|^2$ around AuNR(in) at peak A was higher than that at peak B, which suggests that the coupling efficiency of the mode at peak A is higher than that at peak B (Fig. S6B). In addition, as described above, the confined light in the PCS holes resulting from mode A attracts AuNRs into the holes during the immersion of PCS into the dispersed AuNR solution, which results in the loading of AuNRs into the holes of PCS. In the experimental and simulated evaluations of the hybrid structure, it should be noted that the effects of the different locations and orientations of the AuNRs in the experiment and simulation were considered to be negligible on average. In the experiment, the AuNRs were randomly located and oriented on the PCS while the AuNRs were fixed at the centers of the holes and on top of the PCS surface in the simulation (Fig. 1A and C). In this study, the sensitivity toward the detection of DNA hybridization was evaluated using the two aforementioned coupling modes (denoted by peaks A and B) based on the plasmonic–photonic coupling regime.

3.2. DNA-functionalized AuNR loading onto the PCS

In this study, a 23-base DNA sequence containing a fragment of gene encoding apolipoprotein E (ApoE), which carries a point mutation associated with progression of Alzheimer's disease (ref), including probe, complementary (comp), one-base-mismatched (1-mis), and noncomplementary (mis) DNA molecules, was used to investigate the sensitive detection and identification of DNA using the developed system (Table S1). To achieve this, 5' disulfide-modified probe DNA was first loaded onto the surface of AuNRs using a salt-aging method [43], and an aqueous solution of the probe DNA-modified AuNRs (P-AuNRs) was prepared (see the Materials and Methods section). The absorption peak wavelength of the AuNR-dispersed buffer solution was red-shifted at $9.9 \pm 0.1 \text{ nm}$ (number of samples $N = 3$), which indicates that the probe DNA was immobilized on the surface of the AuNRs (Fig. S7). The PCS surface was incubated in this solution for various loading times ($T_{\text{load}} = 30, 45, 60, 90, \text{ or } 120 \text{ min}$), and the resulting DNA-functionalized hybrid sensors were incubated in the DNA sample solution for 1 h at 37°C (see the Materials and Methods section). A schematic of the experimental process is shown in Fig. 3A, and the spectra obtained during each phase of this process are shown in Fig. 3B and C. The change in peak intensity ($=\Delta R$) was observed during the AuNR loading ($\Delta R_{\text{load}} = R_{\text{PCS}} - R_{\text{hyb}}$) and DNA detection ($\Delta R_{\text{det}} = R_{\text{hyb}} -$

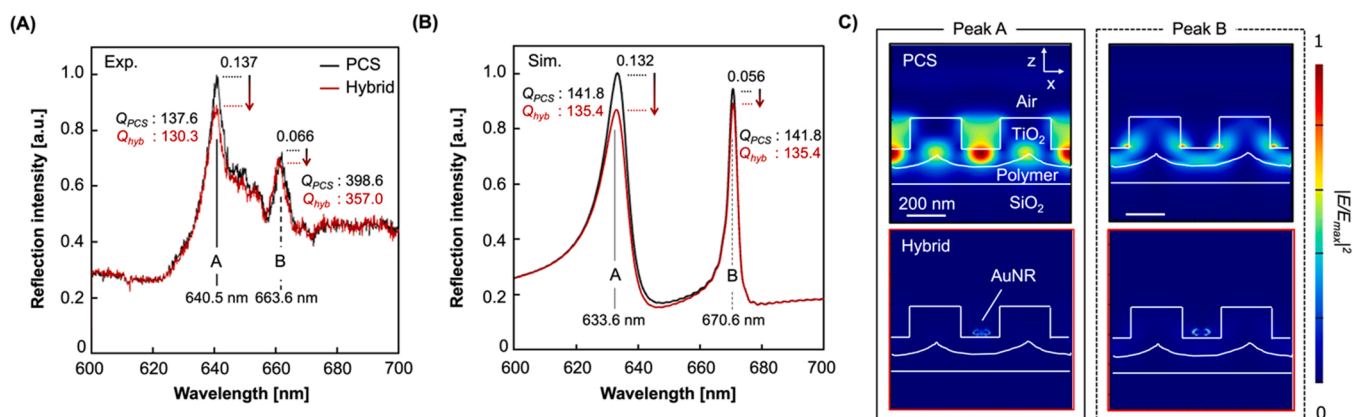


Fig. 2. Optical characterization of plasmonic–photonic hybrid mode. (A) Experimental and (B) simulated reflection spectra of the PCS (black) and hybrid structure (red). Two reflection peaks, denoted as A (solid line) and B (dashed line), are shown in the spectra of the PCS and hybrid. The peak wavelength, change in peak intensity, and Q -factors of the PCS (Q_{PCS}) and hybrid (Q_{Hyb}) for peaks A and B are shown in these figures. The Q -factors were calculated as $Q = \lambda_{\text{peak}}/\text{FWHM}$ by Lorentzian fitting, where FWHM is the full width at half maximum of the peaks. By comparing the PCS to the hybrid, the peak wavelengths did not shift, although the peak intensity and Q -factors decreased. (C) x - z cross-sectional images of the normalized electric field ($|E/E_{\text{max}}|^2$) around AuNR(in) at the peaks A (leftmost solid-square) and B (rightmost dashed-square) of the PCS (top) and the hybrid (bottom). As the PCS serves to provide microcavities, the light was localized in the holes at peak A (mode A), whereas it was localized in the slabs of PCS (mode B) at peak B. Upon hybridization with AuNRs, the light was confined in the AuNRs, which served as nanoantennae, at both modes A and B.

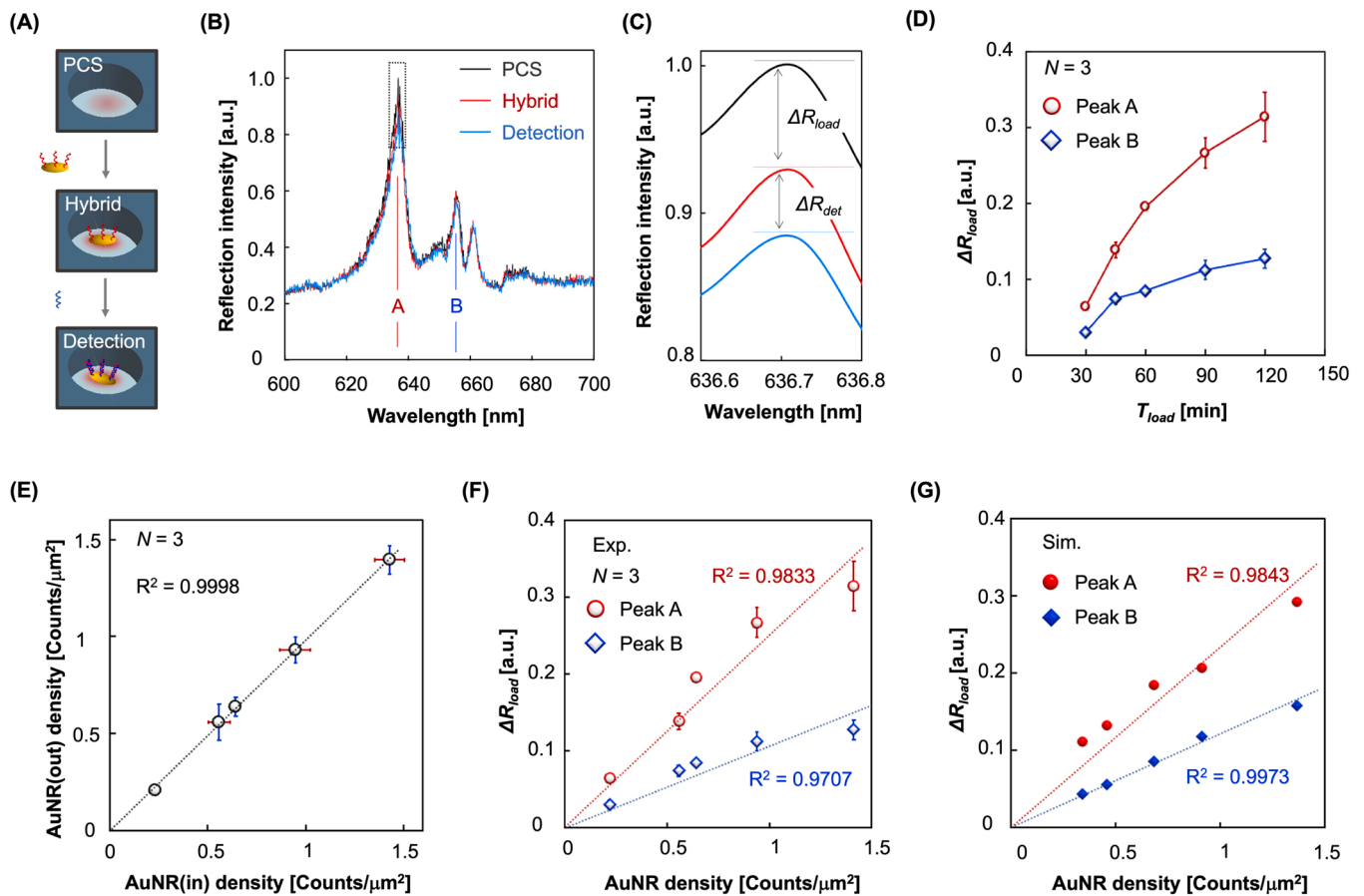


Fig. 3. AuNR loading onto PCS. (A) Schematic illustration of the loading of probe-DNA onto the functionalized AuNR PCS structure (hybrid sensor) and the detection of the target DNA hybridization. (B) Reflection spectra of the PCS (black), hybrid (red), and detection (blue) that correspond to the experimental process in (a). The AuNR loading time T_{load} was 30 min, and a target 1 pM of DNA was used. (C) Expanded view of the reflection peak A (indicated by the dashed-line box in (B)). The decrease in the peak intensity from PCS (R_{PCS}) to hybrid (R_{hyb}) was described as ΔR_{load} ($\Delta R_{load} = R_{PCS} - R_{hyb}$), whereas that from hybrid to detection (R_{det}) was defined as ΔR_{det} ($\Delta R_{det} = R_{hyb} - R_{det}$). (D) Plots of ΔR_{load} versus T_{load} (30, 45, 60, 90, or 120 min) for peaks A (red circles) and B (blue squares) ($N = 3$). (E) Plots of the densities of AuNR(in) and AuNR(out) on the PCS surface area [counts/ μm^2] for each loading time T_{load} ($N = 3$). Nearly identical densities of AuNR(in) and AuNR(out) were confirmed for each T_{load} ($R^2 = 0.9998$), and the final AuNR density was defined as the average of these values. (F) Experimental and (G) simulated plots of ΔR_{load} versus the AuNR density for peaks A (red circles) and B (blue squares). Good linearity for each plot was confirmed ($R^2 > 0.97$), and therefore, ΔR_{load} was considered linearly related to the AuNR density.

R_{det} processes, in which R_{PCS} , R_{hyb} , and R_{det} represent the reflection intensities of the PCS, hybrid sensor, and hybrid sensor after DNA hybridization, respectively. The correlation between T_{load} and ΔR_{load} was evaluated (Fig. 3D). The densities of AuNR(in) and AuNR(out) over the PCS surface area in units of counts/ μm^2 were determined for each loading time based on the SEM images (Fig. 3E, Materials and Methods). For example, considering the SEM images of the hybrid sensors ($T_{load} = 30, 60$ min) shown in Fig. S2, ΔR_{load} increased as T_{load} increased, and peak A showed a more dynamic decrease in ΔR_{load} than peak B. The densities of AuNR(in) and AuNR(out) for each loading time were largely unchanged, as shown in Fig. 3E. These results suggest that the coupling intensity of mode A was higher than that of mode B regardless of the density of AuNRs, as discussed above (Fig. S6). The correlation between the density of the AuNRs, which was taken as the average value of the AuNR(in) and AuNR(out) densities at each loading time, and ΔR_{load} was evaluated using the experimental and simulation results (Fig. 3F and G). The linearity of this relationship could be determined from both the experimental and simulated results. Therefore, in the following evaluation of the optical properties of the hybrid sensors, ΔR_{load} was measured and used as a parameter related to the density of the AuNRs. In addition, a good agreement between experimental and simulation results was confirmed, although the distributions of the AuNRs on the PCS varied between the experiment and simulation. This agreement suggests

that the average distribution of AuNRs in the experimental hybrid structure was similar to that of the simulated model, and therefore the detailed optical properties of the experimental hybrid structure could be evaluated using the simulation model.

3.3. Plasmonic–photonic hybrid sensor for label-free DNA detection

The sensitivity of the developed hybrid sensor for DNA hybridization detection was experimentally evaluated next. For the detection of DNA hybridization, the reflection intensities of peaks A and B were measured before and after incubation of the hybrid sensor in the comp-DNA sample solution (1 pM), and the response of the system ΔR_{det} ($\Delta R_{det} = R_{hyb} - R_{det}$) was analyzed. The sensitivity S , which is defined by the ratio of ΔR_{det} to ΔR_{load} ($S = \Delta R_{det} / \Delta R_{load}$) and expresses the response of the system per unit of AuNRs, was then calculated. As the linearity between the AuNR density and ΔR_{load} was estimated in Fig. 3F and G, the sensitivity S indicates the response per unit of AuNR(in) and AuNR(out). The response ΔR_{det} and S to ΔR_{load} were plotted in Fig. 4A and B, respectively. Each plot is shown with respect to varied ΔR_{load} values that correspond to T_{load} values at 30, 45, 60, 90, or 120 min. The response, ΔR_{det} of both peaks A and B showed maximum values with respect to ΔR_{load} and the loading time T_{load} . The significant difference in the dynamic ranges of the responses of modes A and B may be attributed to the

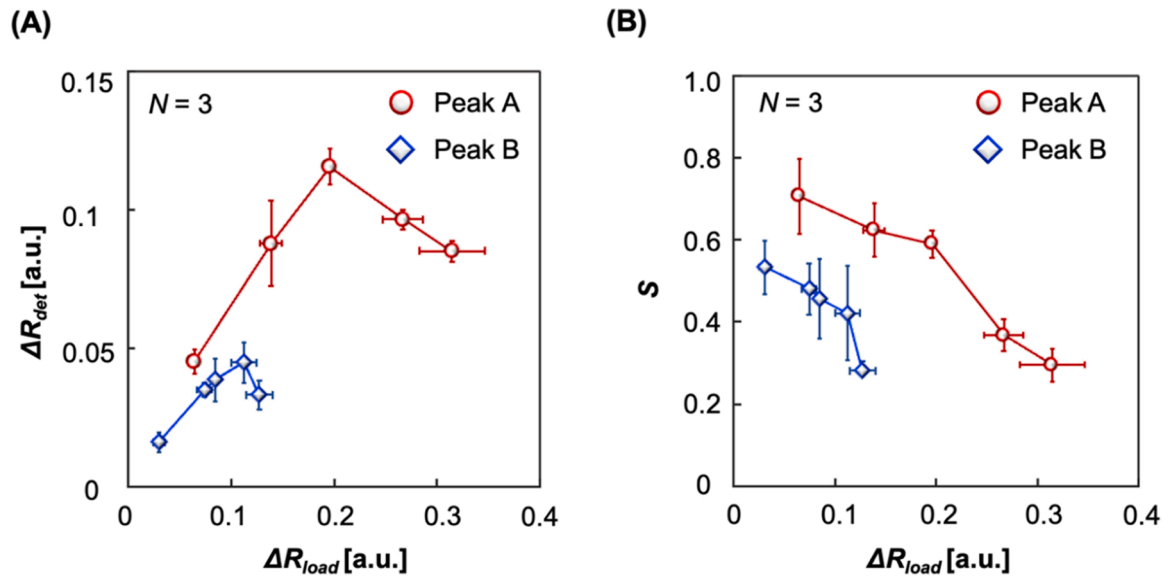


Fig. 4. Plasmonic-photonic hybrid sensor for DNA detection. (A) Plots of the response (ΔR_{det}) toward DNA hybridization (1 pM) versus ΔR_{load} , which was obtained from the series of loading times T_{load} ($N = 3$). The red circles and blue squares correspond to peaks A and B, respectively. (B) Plots of sensitivity S ($S = \Delta R_{det}/\Delta R_{load}$), which indicates the responsivity per unit of AuNR(in) and AuNR(out), versus ΔR_{load} ($N = 3$). The red circles and blue squares correspond to peaks A and B, respectively.

mode coupling efficiency between nanoantennae and microcavities. Here, a higher plasmonic-photonic coupling intensity would result in a larger response of the system toward DNA hybridization. The sensitivity S decreased as ΔR_{load} increased. For each loading time, ΔR_{det} and S of peak A were higher than those of peak B, which may also be attributed to the difference in mode coupling efficiencies between these peaks. The error bars of ΔR_{load} and S may result from the following phenomena. At peak A, a higher AuNR density may reduce the coupling efficiency of this mode²⁶, and the sensitivity of the system will be less susceptible to variations in the AuNR density. Conversely, at peak B, the SNR of the peak intensity was too small to clearly demonstrate the trends in the error bars related to the AuNR density (Fig. 2C). The response of this system toward DNA hybridization may have resulted from the additional dissipative loss in the hybrid mode induced by DNA hybridization on the surface of the AuNRs.

3.4. Theoretical model of the plasmonic-photonic hybrid sensor

Next, we theoretically evaluated the plasmonic-photonic coupling mode and constructed a theoretical model of the plasmonic-photonic hybrid sensor. The correlation between the sensitivities and coupling modes at peaks A and B was evaluated based on FDTD calculations, and a theoretical model of the plasmonic-photonic hybrid sensor was then constructed based on the TCMT^[26,32–34]. Liu et al. previously applied TCMT for a nanoantenna-microcavity hybrid system^[26,32–34]. We modified TCMT for application toward our hybrid sensor (Text S1). The average near-field intensities $\langle |E_{in}|^2 \rangle$ and $\langle |E_{out}|^2 \rangle$ around the surfaces of AuNR(in) and AuNR(out), respectively, were calculated using the FDTD method, and the near-field intensity $\langle |E|^2 \rangle$ is defined as the sum of $\langle |E_{in}|^2 \rangle$ and $\langle |E_{out}|^2 \rangle$ (i.e., $\langle |E|^2 \rangle = \langle |E_{in}|^2 \rangle + \langle |E_{out}|^2 \rangle$). When the perturbations between the two resonant systems of AuNR(in) and AuNR(out) are ignored⁽³¹⁾, the optical energy $|a|^2$ stored in the hybrid system at the resonance frequency $\omega = \omega_0$ considering the near-field intensity $\langle |E|^2 \rangle$ can be described as:

$$|a|^2 \equiv \frac{1}{2} \epsilon_0 \langle |E|^2 \rangle V_{eff} \quad (1)$$

where V_{eff} is the effective modal volume. Here, the V_{eff} values of modes A and B are considered to be the same because this quantity mainly depends on the AuNR volume. The dissipation power P_{abs} at resonance is described as:

$$P_{abs} = -\frac{d}{dt} |a|^2 \Big|_{abs} = 2\gamma_{abs} |a|^2 \quad (2)$$

The dissipation power P_{abs} may then written as:

$$P_{abs} \propto \gamma_{abs} \langle |E|^2 \rangle \quad (3)$$

When the absorption loss rate γ_{abs} in the hybrid system is increased owing to fluctuations or perturbations in the surface electron states of the nanoantennae due to DNA hybridization on the AuNR surface, the change in the rate of absorption, which is expected to be related to the sensitivity S , can be described as:

$$S \propto \frac{dP_{abs}}{d\gamma_{abs}} \propto \langle |E|^2 \rangle \quad (4)$$

Conversely, based on the application of TMCT to our hybrid system, the near-field intensity can be expressed using the Q-factors of the PCS (Q_{PCS}) and hybrid (Q_{hyb}), as:

$$\langle |E|^2 \rangle \propto \frac{Q_{hyb}^2}{Q_{PCS}} \quad (5)$$

The near-field intensity $\langle |E|^2 \rangle$ and Q_{hyb}^2/Q_{PCS} values at peaks A and B were plotted for each AuNR density, as shown in Fig. 5A and B, respectively. The Q-factor of the hybrid system is defined as $Q_{hyb} = (Q_{rad}^{-1} + Q_{abs}^{-1})^{-1}$, where Q_{rad} and Q_{abs} are the radiation and dissipation quality factors, respectively, and $Q_{rad} \approx Q_{PCS}$. Q_{hyb} was observed to decrease as the absorption Q-factor (Q_{abs}) decreased due to the dissipation losses of the AuNRs (Text S2). Therefore, the decreases in both $\langle |E|^2 \rangle$ and Q_{hyb}^2/Q_{PCS} demonstrated that the hybrid system was well explained using TCMT. At peak A, the near-field intensity was decreased more drastically than at peak B. This result suggests that the plasmonic-photonic coupling efficiency of mode A is greater than that of mode B owing to the larger spatial and spectral overlaps between the modes of the AuNRs and PCS. Fig. 5C shows the calculated near-field intensity

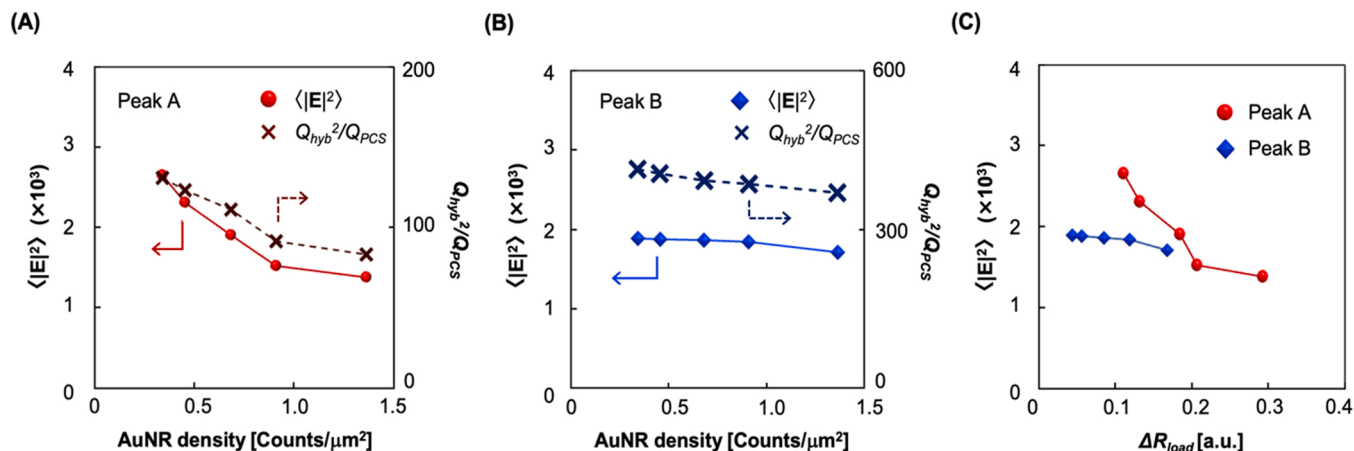


Fig. 5. Theoretical model results of the plasmonic-photonic hybrid sensor based on the temporal coupled-mode theory (TCMT). (A), (B) Correlation between the near-field intensity ($\langle |E|^2 \rangle = \langle |E_{in}|^2 \rangle + \langle |E_{out}|^2 \rangle$) around the surface of the AuNRs ($\langle |E_{in}|^2 \rangle$ for AuNR(in) and $\langle |E_{out}|^2 \rangle$ for AuNR(out)) and Q_{hyb}^2/Q_{PCS} , which is the TCMT-based parameter correlated with the near-field intensity ($\langle |E|^2 \rangle \propto Q_{hyb}^2/Q_{PCS}$) at peaks A and B. A good agreement was observed between the trends of these two factors, which decreased as the AuNR density increased, thereby supporting the validity of the TCMT-based model to well represent the hybrid structure. (C) Plots of the near-field intensity $\langle |E|^2 \rangle$, which was considered to be correlated with the sensitivity $S \propto dP_{abs}/d\gamma_{abs} \propto \langle |E|^2 \rangle$, where P_{abs} is the dissipation power, and γ_{abs} is the dissipation rate in the hybrid system. S was defined as the change in absorption power due to the change in the dissipation loss rate resulting from the adsorption of the DNA double strands onto the AuNR surface. The plots of the near-field intensity $\langle |E|^2 \rangle$ are in good agreement with the sensitivity S results shown in Fig. 3B.

$\langle |E|^2 \rangle$ for ΔR_{load} , which corresponds to the AuNR density. A good agreement is observed between the sensitivity S in the experiment (Fig. 4B) and the near-field intensity $\langle |E|^2 \rangle$ obtained from the simulation, which is considered to be related to the sensitivity. The perturbations between the AuNRs were ignored in the theoretical model constructed using TCMT. However, by comparing the sensitivity S in Fig. 4B and the near-field intensity $\langle |E|^2 \rangle$ in Fig. 5C, it is observed that the perturbations caused by the dense AuNRs may degrade the sensitivity observed in the experimental results. Therefore, our hybrid system model constructed using TCMT well describes our hybrid sensor within the range of an adequately low AuNR density such that perturbations do not occur. According to the TCMT-based theoretical model, the sensitivity of the hybrid sensor was described by the increase in the absorption losses in the plasmonic-photonic hybrid mode, and the absorption losses in the nanoantenna were increased by the DNA molecules on the surface. That is, the deposition of the double strands of DNA on the surface of a gold nanostructure would degrade the LSP resonance owing to the expansion of the electron clouds, and increase losses in the plasmonic-photonic coupling mode. Therefore, the sensitivity S of the developed system is believed to correlate with the plasmonic-photonic coupling mode. In addition, those experimental and theoretical study of the hybrid sensor revealed that the spatial and spectral overlaps between the nanoantennae and microcavities affected the mode coupling efficiency of the overall system, wherein larger overlaps resulted in larger near-field intensities and sensitivities.

3.5. Ultrasensitive label-free detection and identification of DNA using the hybrid sensor

Here, we demonstrate the sensitive detection of DNA hybridization and the identification of single nucleotide mismatched DNA using our hybrid sensor. First, hybrid sensors were fabricated using three different AuNR loading times (T_{load}) of 30, 60, and 90 min. The responses of the hybrid sensor toward the comp-DNA, 1-mis-DNA, and mis-DNA were measured, and their sensitivities were subsequently calculated (Fig. 6A and B). In the subsequent experiments, we evaluated the sensor

properties using mode A because the errors in the reflection intensity observed at mode B were too greatly varied for sensor applications due to the low SNR. Considering 1-mis-DNA, the responsivity of the system was maximum when T_{load} was 60 min, and the sensitivity decreased as T_{load} increased. A similar trend was observed for comp-DNA. This agreement between the trends of the responsivity and sensitivity suggests that the theoretical mechanism for comp-DNA detection could also be applied toward 1-mis-DNA detection. The p-values of mis-, 1-mis-, and comp-DNA were evaluated at levels of $p < 0.05$ and $p < 0.01$. Minimum p-values were observed at a T_{load} of 60 min because the relative standard deviations (RSDs) of the sensitivity were also minimum $T_{load} = 60$ min (Fig. S8). At low AuNR densities ($\Delta R_{load} \leq 60$), the sensitivity was affected by increases in the absorption losses caused by the AuNRs, which indicates that a slight variation in the AuNR density would have a large effect on the sensitivity (Fig. 4B). Conversely, at higher AuNR densities ($60 < \Delta R_{load}$), the density of the AuNRs was more difficult to control (Fig. 3D), and therefore, the sensitivity variation was large (Fig. 4B). Regardless of the variation in the RSD, however, the ratio of the sensitivity of 1-mis-DNA (S_{1-mis}) to that of comp-DNA (S_{comp}) represented by S_{1-mis}/S_{comp} was almost constant at an average value of 0.62 ± 0.01 as T_{load} was varied, which indicated that the sensitivities of comp-DNA and 1-mis-DNA do not vary according to the AuNR density. The observed responses of these systems toward mis-DNA were affected by the non-specific adsorption of mis-DNA onto the surfaces of AuNR and PCS. Therefore, we additionally investigated the physical adsorption of comp-DNA onto the PCS surface. When pristine PCS was incubated in the comp-DNA sample solution using the same procedure as described for the above experiment, the peak intensity slightly decreased to 0.014 ± 0.007 ($N = 3$; $\sim 10\%$ vs. ΔR_{det} for comp-DNA ($T_{load} = 60$ min)), which suggests the adsorption of a small amount of DNA molecules onto the PCS surface. Because this value was close to the response ΔR_{det} for mis-DNA, the apparent response for mis-DNA was attributed to the non-specific adsorption of mis-DNA onto the PCS surface. The capability for identifying single nucleotide mismatched DNA may be attributed to two factors: (a) the efficiency of DNA hybridization differs between comp-DNA and 1-mis-DNA, as previously reported by Peterson et al. [45]; and (b) the dissipation loss caused by the expanded electron clouds owing to the adsorption of double-stranded DNA on the

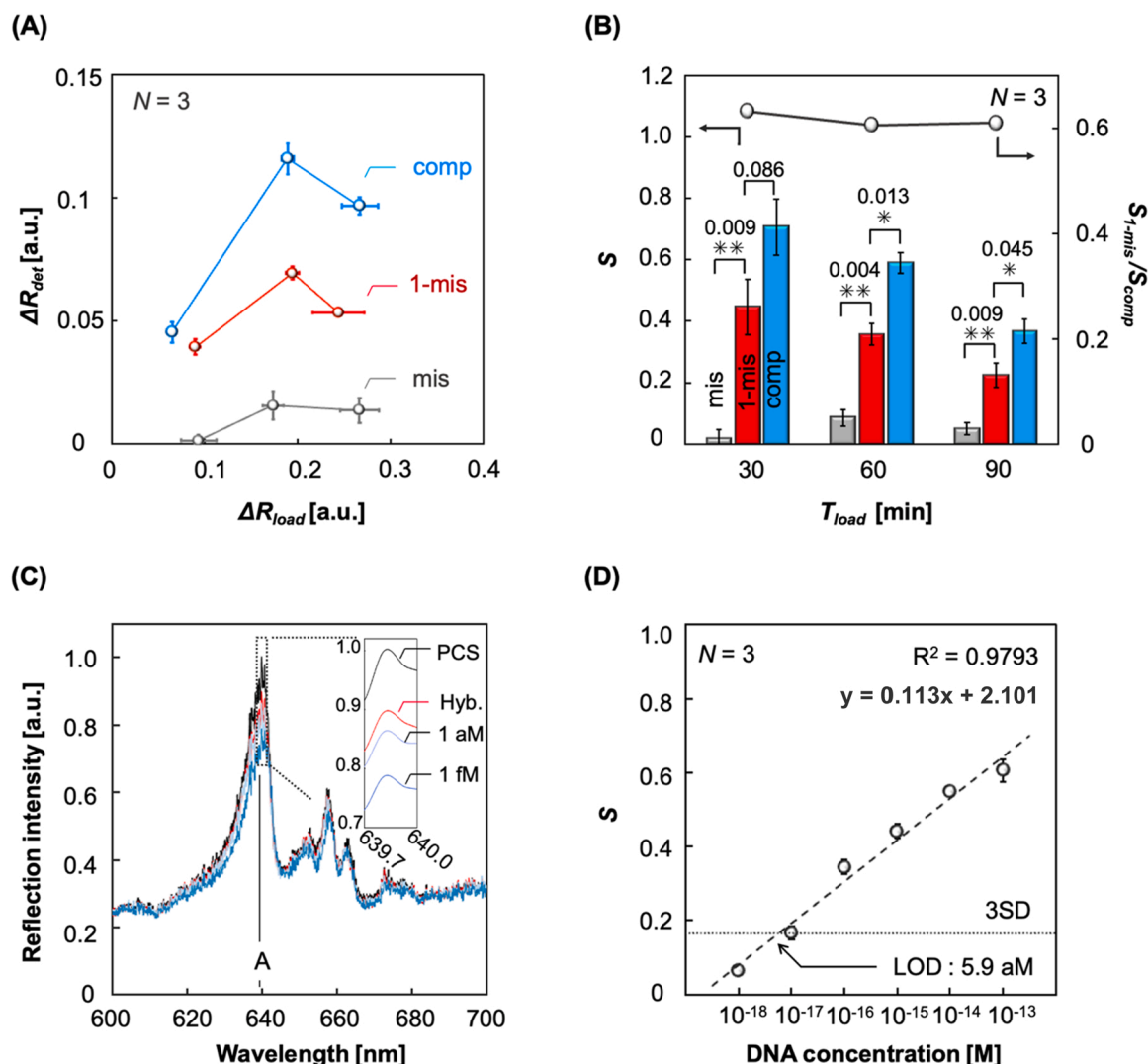


Fig. 6. Ultrasensitive label-free detection and identification of DNA using the hybrid sensor. (A) Response ΔR_{def} for the complementary (comp, sky-blue line), 1-base-mismatched (1-mis, red line), and mismatched (mis, gray line) DNA samples (1 pM) versus ΔR_{load} , obtained from a series of loading times T_{load} (30, 60, and 90 min) ($N = 3$). The dataset of comp-DNA was extracted from the dataset shown in Fig. 3a. (B) Sensitivity S of the developed system for mis-DNA (gray bars), 1-mis-DNA (red bars), and comp-DNA (sky-blue bars), as well as the ratio of the sensitivity of comp-DNA to 1-mis-DNA ($S_{1\text{-mis}}/S_{\text{comp}}$) obtained at each loading time T_{load} . The value of $S_{1\text{-mis}}/S_{\text{comp}}$ did not vary greatly (0.62 ± 0.01), suggesting that the nanoantennae could consistently identify and differentiate 1-mis-DNA from comp-DNA regardless of the AuNR density. T-tests were performed, and p-values were evaluated. * $p < 0.05$; ** $p < 0.01$. (C) Typical reflection spectra of the PCS (black) and hybrid before (red) and after 1-aM (light blue) and 1-fM (dark blue) comp-DNA detection. (Inset: enlarged spectra extracted from the dashed square region.) (D) Calibration line of the sensitivity S for DNA concentrations in the range from 1 aM to 100 fM. The 3-times standard deviation (3 SD) line (dashed line) is shown, and the limit of detection (LOD) based on the 3 SD line is 5.9 aM (~ 1000 molecules). Triplicate measurements were conducted ($N = 3$).

AuNR surface is smaller for 1-mis-DNA than for comp-DNA. This occurs because the single nucleotide mismatched component disconnects the electron orbital that extends from the AuNR surface to the double-stranded DNA, resulting in a lower dissipation loss and sensitivity toward DNA hybridization [36–39]. The lower number of mismatched base-pairs results in higher hybridization efficiencies, and a larger distance between the mismatched base pair and the nanoantenna surface results in less absorption losses in the hybridization mode, thereby producing a higher responsivity. Next, the calibration of our hybrid sensor ($T_{\text{load}} = 60$ min) toward comp-DNA was evaluated at a DNA concentration range of 1 aM to 100 fM. Fig. 6C shows the changes in the reflection spectra that occurred as a result of this variation. As the concentration of the DNA sample solutions increased, the reflection intensity decreased. The reflection spectra in the cases of 1 aM and 1 fM of comp-DNA are also shown in Fig. 6C. The calibration curve for the sensitivity of this system toward various DNA concentrations C [M] was then determined, as shown in Fig. 6D. The good linearity of this curve for

the quantification of DNA samples in this dynamic range ($R^2 = 0.9793$) was confirmed, and a very low LOD of 5.9 aM (~ 1000 molecules) was estimated from the three standard deviation (3 SD) line. The resolution of S value as signal with the detector was less than 10^{-5} , which gives the theoretical resolution of logarithm concentration of molecules (Log M) less than 10^{-4} , according to the approximate line. Then, the resolution of signal was high enough to achieve the approximate LOD value. It should be noted that this low LOD was successfully achieved using a simple microscopic method, as shown in Fig. 1B. However, our hybrid sensor seems to have potential for improvement in its sensitivity and accuracy. The reflectometric measurement using broadband-white light might reduce photonic signal-to-noise ratio because of the broadband 0-mode reflection, and inflate the apparent sensitivity because of spurious reflection which was distributed to the low quality of the photonic cavity. The improvement in fabrication process using nano-imprint techniques can give high quality PCS, and single-frequency excitation will increase photonic signal-to-noise ratio. We should

investigate these aspects for further improvement in our sensor.

4. Conclusions

We developed a plasmonic–photonic hybrid sensor that may be used for label-free and ultrasensitive analysis of biomolecules via simple and facile microspectroscopy. Several unique and important achievements were obtained with our hybrid sensor. First, our hybrid sensor was fabricated using a simple and high-throughput process via nanoimprint lithography. Therefore, this coupled mode tunable hybrid sensor may be rapidly and simply produced on a large scale. AuNRs as nanoantennae were controllably loaded onto PCS, which enabled the tuning of the plasmonic–photonic coupling efficiency and the experimental evaluation of the correlation between the sensitivity and mode coupling efficiency. Earlier, it was challenging to quantitate the sensitivity of conventional sensors because of several difficulties and complications related to the fabrication and tuning of hybrid structures [22–25]. Our easy-to-produce hybrid sensor overcomes these challenges. Moreover, a theoretical model of our hybrid sensor was constructed based on the TCMT. According to the constructed model, the sensitivity of hybrid sensor may be evaluated by assessing the near-field intensity around the AuNRs at the plasmonic–photonic resonance, and a good agreement between the sensitivity from the experimental results and the near-field intensity calculated by the FDTD method was achieved. In addition, a good correlation between the TCMT-based factor Q_{hyb}^2/Q_{PCS} , which is used to describe the hybrid system, and the near-field intensity was confirmed. This agreement provided evidence that the constructed TCMT-based theoretical model correctly determines the sensitivity of the hybrid sensor. The key finding from the theoretical model of the plasmonic–photonic hybrid sensor is that the sensitivity is correlated with the absorption losses in the plasmonic–photonic hybrid mode and described by the near-field intensity around the nanoantenna. The absorption losses of the hybrid mode are increased owing to the molecules adsorbed on the nanoantenna surface, thus the hybrid sensor response to the molecular events caused on the AuNR surface. Another unique finding is that the spatial and spectral overlaps between the nanoantennae and microcavities affected the mode coupling efficiency of the overall system, wherein larger overlaps resulted in larger near-field intensities and sensitivities. Finally, our hybrid sensor demonstrated ultrasensitive detection of DNA hybridization and identified the single nucleotide mismatched DNA sequence of *ApoE* related to the progression of Alzheimer's disease. We also successfully achieved an ultralow LOD (3 SD) of 5.9 aM (~1000 molecules) using a simple and cost-effective spectroscopic method [40–42]. A typical optical microscope was used for the reflectometric analysis conducted with our hybrid sensor, thereby demonstrating the high usability and wide applicability of the developed system, which may be applied in fields such as biomedical science and medical diagnosis. In conclusion, with the developed hybrid sensor, we revealed the mechanism underlying the label-free detection of biomolecules using the plasmonic–photonic hybrid mode and demonstrated the ultrasensitive detection of DNA hybridization based on a simple and facile spectroscopic method. The high sensitivity of our hybrid sensor resulted from the extremely enhanced near-field generated by the cooperative plasmonic–photonic coupling resonance, which was achieved using the simply and easily fabricated hybrid structure. Our sensor may be used to conduct more detailed experimental investigations of plasmonic–photonic hybrid structures, as well as in the further development of label-free optical bioanalysis methods for use in the biological and medical science fields.

Funding

This work was supported by the Japan Society for the Promotion of Science (JSPS).

CRedit authorship contribution statement

Daiki Kawasaki: Writing – original draft, Investigation, Methodology, Visualization. **Hirotaka Yamada:** Methodology, Software. **Kenji Sueyoshi:** Writing – review & editing. **Hideaki Hisamoto:** Writing – review & editing. **Tatsuro Endo:** Conceptualization, Supervision, Writing – original draft, Writing – review & editing.

Author contributions

D.K. designed and conducted the experiments. **H.Y., K.S., H.H., and T.E.** conceived of and advised the experiments. **D.K., H.H., and T.E.** wrote the paper.

Declaration of Competing Interest

The authors declare the following financial interests/personal relationships which may be considered as potential competing interests: Tatsuro Endo reports financial support was provided by Ministry of Education, Culture, Sports, Science and Technology.

Acknowledgement

This work was supported by the Japan Society for the Promotion of Science (JSPS).

Supporting Information

Theoretical models of the hybrid sensor, SEM images, and other analysis results.

Appendix A. Supporting information

Supplementary data associated with this article can be found in the online version at doi:10.1016/j.snb.2022.131747.

References

- [1] Y. Chen, J. Liu, Z. Yang, J.S. Wilkinson, X. Zhou, Optical biosensors based on refractometric sensing schemes: a review, *Biosens. Bioelectron.* 144 (2019), 111693, <https://doi.org/10.1016/j.bios.2019.111693>.
- [2] X. Fan, I.M. White, S.I. Shopova, H. Zhu, J.D. Suter, Y. Sun, Sensitive optical biosensors for unlabeled targets: a review, *Anal. Chim. Acta* 620 (2008) 8–26, <https://doi.org/10.1016/j.aca.2008.05.022>.
- [3] P.B. Lippa, L.J. Sokoll, D.W. Chan, Immunosensors - principles and applications to clinical chemistry, *Clin. Chim. Acta* 314 (2001) 1–26, [https://doi.org/10.1016/S0009-8981\(01\)00629-5](https://doi.org/10.1016/S0009-8981(01)00629-5).
- [4] M. Kaisti, Detection principles of biological and chemical FET sensors, *Biosens. Bioelectron.* 98 (2017) 437–448, <https://doi.org/10.1016/j.bios.2017.07.010>.
- [5] Y. Cui, Q. Wei, H. Park, C.M. Lieber, Nanowire nanosensors for highly sensitive and selective detection of biological and chemical species, *Science* 293 (2001) 1289–1292, <https://doi.org/10.1126/science.1062711>.
- [6] M. Di Ventra, M. Taniguchi, Decoding DNA, RNA and peptides with quantum tunnelling, *Nat. Nanotechnol.* 11 (2016) 117–126, <https://doi.org/10.1038/nnano.2015.320>.
- [7] A.P. Ivanov, E. Instuli, C.M. McGilvery, G. Baldwin, D.W. McComb, T. Albrecht, J. B. Edel, DNA tunneling detector embedded in a nanopore, *Nano Lett.* 11 (2011) 279–285, <https://doi.org/10.1021/nl103873a>.
- [8] E. Luan, H. Shoman, D.M. Ratner, K.C. Cheung, L. Chrostowski, Silicon photonic biosensors using label-free detection, *Sensors* 18 (2018) 1–42, <https://doi.org/10.3390/s18103519>.
- [9] D.J. Stephens, V.J. Allan, Light microscopy techniques for live cell imaging, *Science* 300 (2003) 82–86, <https://doi.org/10.1126/science.1082160>.
- [10] L. Tang, J. Li, Plasmon-based colorimetric nanosensors for ultrasensitive molecular diagnostics, *ACS Sens.* 2 (2017) 857–875, <https://doi.org/10.1021/acssensors.7b00282>.
- [11] M.A. Cooper, Optical biosensors in drug discovery, *Nat. Rev. Drug Discov.* 1 (2002) 515–528, <https://doi.org/10.1038/nrd838>.
- [12] J.A. Schuller, E.S. Barnard, W. Cai, Y.C. Jun, J. White, Mark L. Brongersma, Plasmonics for extreme light concentration and manipulation, *Nat. Mater.* 9 (2010) 193–204.
- [13] S. Schlücker, Surface-enhanced raman spectroscopy: Concepts and chemical applications, *Angew. Chem. Int. Ed.* 53 (2014) 4756–4795, <https://doi.org/10.1002/anie.201205748>.

- [14] K.A. Willets, R.P. Van Duyne, Localized surface plasmon resonance spectroscopy and sensing, *Annu. Rev. Phys. Chem.* 58 (2007) 267–297.
- [15] K.V. Sreekanth, Y. Alapan, M. ElKabbash, E. Ilker, M. Hinczewski, U.A. Gurkan, A. De Luca, G. Strangi, Extreme sensitivity biosensing platform based on hyperbolic metamaterials, *Nat. Mater.* 15 (2016) 621, <https://doi.org/10.1038/nmat4609>.
- [16] A. Habib, X. Zhu, U.I. Can, M.L. McLanahan, P. Zorlutuna, A.A. Yanik, Electro-plasmonic nanoantenna: a nonfluorescent optical probe for ultrasensitive label-free detection of electrophysiological signals, *Sci. Adv.* 5 (2019), <https://doi.org/10.1126/sciadv.aav9786>.
- [17] T. Chung, S. Lee, E.Y. Song, H. Chun, B. Lee, Plasmonic nanostructures for nano-scale bio-sensing, *Sensors* 11 (2011) 10907–10929.
- [18] C. Dekker, D.V. Verschuere, S. Pud, X. Shi, L. De Angelis, L. Kuipers, Label-free optical detection of DNA translocations through plasmonic nanopores, *ACS Nano* 13 (2019) 61–70, <https://doi.org/10.1021/acsnano.8b06758>.
- [19] P.R. West, S. Ishii, G.V. Naik, N.K. Emani, V.M. Shalae, Searching for better plasmonic materials, *Laser Photonics Rev.* 4 (2010) 795–808.
- [20] B. Doiron, M. Mota, M.P. Wells, R. Bower, A. Mihai, Y. Li, L.F. Cohen, N.M. Alford, P.K. Petrov, R.F. Oulton, S.A. Maier, Quantifying figures of merit for localized surface plasmon resonance applications: a materials survey, *ACS Photonics* 10 (2019) 1–20.
- [21] M.A. Santiago-Cordoba, S.V. Boriskina, F. Vollmer, M.C. Demirel, Nanoparticle-based protein detection by optical shift of a resonant microcavity, *Appl. Phys. Lett.* 99 (2011) 2009–2012, <https://doi.org/10.1063/1.3599706>.
- [22] F. De Angelis, M. Patrini, G. Das, I. Maksymov, M. Galli, L. Businaro, L.C. Andreani, E. Di Fabrizio, A hybrid plasmonic - photonic nanodevice for label-free detection of a few molecules, *Nano Lett.* 8 (2008) 2321–2327.
- [23] F. Liang, Y. Guo, S. Hou, Q. Quan, Photonic-plasmonic hybrid single-molecule nanosensor measures the effect of fluorescent labels on DNA-protein dynamics, *Sci. Adv.* 3 (2017) 1–11.
- [24] J.D. Swaim, J. Knittel, W.P. Bowen, Detection limits in whispering gallery biosensors with plasmonic enhancement, *Appl. Phys. Lett.* 99 (2011) 1–4, <https://doi.org/10.1063/1.3669398>.
- [25] M. Barth, S. Schietinger, S. Fischer, J. Becker, N. Nüsse, T. Aichele, B. Löchel, C. Sönnichsen, O. Benson, Nanoassembled plasmonic-photonic hybrid cavity for tailored light-matter coupling, *Nano Lett.* 10 (2010) 891–895, <https://doi.org/10.1021/nl903555u>.
- [26] J. Liu, Q. Huang, K. Liu, S. Singamaneni, B.T. Cunningham, Nanoantenna – microcavity hybrids with highly cooperative plasmonic – photonic coupling, *Nano Lett.* 17 (2017) 7568–7577.
- [27] D. Kawasaki, H. Yamada, K. Maeno, K. Sueyoshi, H. Hisamoto, T. Endo, Core-shell-structured gold nanocone array for label-free DNA sensing, *ACS Appl. Nano Mater.* 2 (2019) 4983–4990, <https://doi.org/10.1021/acsnano.9b00930>.
- [28] D. Kawasaki, K. Maeno, H. Yamada, K. Sueyoshi, H. Hisamoto, T. Endo, TiN-contained polymer-metal core-shell structured nanocone array: engineering of sensor performance by controlling plasmonic properties, *Sens. Actuators B Chem.* 299 (2019), 126932, <https://doi.org/10.1016/j.snb.2019.126932>.
- [29] W.J. Strittmatter, A.M. Saunders, D. Schmechel, M. Pericak-Vance, J. Enghild, G. S. Salvesen, A.D. Roses, Apolipoprotein E: high-avidity binding to β -amyloid and increased frequency of type 4 allele in late-onset familial Alzheimer disease, *Proc. Natl. Acad. Sci. USA* 90 (1993) 1977–1981, <https://doi.org/10.1073/pnas.90.5.1977>.
- [30] J.E. Hixson, D.T. Vernier, Restriction isotyping of human apolipoprotein E by gene amplification and cleavage with *HhaI*, *J. Lipid Res.* 31 (1990) 545–548, [https://doi.org/10.1016/s0022-2275\(20\)43176-1](https://doi.org/10.1016/s0022-2275(20)43176-1).
- [31] D. Kawasaki, R. Oishi, N. Kobayashi, T. Mizuta, K. Sueyoshi, H. Hisamoto, T. Endo, Highly sensitive optical ion sensor with ionic liquid-based colorimetric membrane/photonic crystal hybrid structure, *Sci. Rep.* 10 (2020) 1–10, <https://doi.org/10.1038/s41598-020-73858-8>.
- [32] W. Suh, Z. Wang, S. Fan, Temporal coupled-mode theory and the presence of non-orthogonal modes in lossless multimode cavities, *IEEE J. Quantum Electron.* 40 (2004) 1511–1518, <https://doi.org/10.1109/JQE.2004.834773>.
- [33] C. Batchelor, J. Hastings, Waves and Fields in Optoelectronics, 1984.
- [34] T.J. Seok, A. Jamshidi, M. Kim, S. Dhuey, A. Lakhani, H. Choo, P.J. Schuck, S. Cabrini, A.M. Schwartzberg, J. Bokor, E. Yablonovitch, M.C. Wu, Radiation engineering of optical antennas for maximum field enhancement, *Nano Lett.* 11 (2011) 2606–2610, <https://doi.org/10.1021/nl2010862>.
- [35] J. A. Stratton, *Electromagnetic Theory*, McGraw-Hill, 1941, <https://doi.org/10.1134/S0040601507080046>.
- [36] T. Liyanage, A.N. Masterson, H.H. Oyem, H. Kaimaklitis, H. Nguyen, R. Sardar, Plasmoelectronic-based ultrasensitive assay of tumor suppressor microRNAs directly in patient plasma: design of highly specific early cancer diagnostic technology, *Anal. Chem.* 91 (2019) 1894–1903, <https://doi.org/10.1021/acs.analchem.8b03768>.
- [37] S.L. Westcott, R.D. Averitt, J.A. Wolfgang, P. Nordlander, N.J. Halas, Adsorbate-induced quenching of hot electrons in gold core-shell nanoparticles, *J. Phys. Chem. B* 105 (2001) 9913–9917, <https://doi.org/10.1021/jp011213t>.
- [38] B.N.J. Persson, Polarizability of small spherical metal particles: influence of the matrix environment, *Surf. Sci.* 281 (1993) 153–162, [https://doi.org/10.1016/0039-6028\(93\)90865-H](https://doi.org/10.1016/0039-6028(93)90865-H).
- [39] B. Foerster, V.A. Spata, E.A. Carter, C. Sönnichsen, S. Link, Plasmon damping depends on the chemical nature of the nanoparticle interface, *Sci. Adv.* 5 (2019) 1–6, <https://doi.org/10.1126/sciadv.aav0704>.
- [40] A. Bonyár, Label-free nucleic acid biosensing using nanomaterial-based localized surface plasmon resonance imaging: a review, *ACS Appl. Nano Mater.* 3 (2020) 8506–8521, <https://doi.org/10.1021/acsnano.0c01457>.
- [41] K. Vikrant, N. Bhardwaj, S.K. Bhardwaj, K.H. Kim, A. Deep, Nanomaterials as efficient platforms for sensing DNA, *Biomaterials* 214 (2019), <https://doi.org/10.1016/j.biomaterials.2019.05.026>.
- [42] D. Sadighbayan, M. Hasanazadeh, E. Ghafar-Zadeh, Biosensing based on field-effect transistors (FET): recent progress and challenges, *TrAC Trends Anal. Chem.* 133 (2020), 116067, <https://doi.org/10.1016/j.trac.2020.116067>.
- [43] S.J. Hurst, A.K.R. Lytton-Jean, C.A. Mirkin, Maximizing DNA loading on a range of gold nanoparticle sizes, *Anal. Chem.* 78 (2006) 8313–8318, <https://doi.org/10.1021/ac0613582>.
- [44] O.M. Maragò, P.H. Jones, P.G. Gucciardi, G. Volpe, A.C. Ferrari, Optical trapping and manipulation of nanostructures, *Nat. Nanotechnol.* 8 (2013) 807–819, <https://doi.org/10.1038/nnano.2013.208>.
- [45] A.W. Peterson, L.K. Wolf, R.M. Georgiadis, Hybridization of mismatched or partially matched DNA at surfaces, *J. Am. Chem. Soc.* 124 (2002) 14601–14607, <https://doi.org/10.1021/ja0279996>.

Daiki Kawasaki received his Master's degree in Applied Chemistry from Osaka Prefecture University (Japan) in 2020. In 2020, he entered the doctoral course of the Graduate School of Engineering Osaka Prefecture University.

Hirotaka Yamada received his Master's degree in Applied Chemistry from Osaka Prefecture University (Japan) in 2019. In 2019, he entered the doctoral course of the Graduate School of Engineering Osaka Prefecture University.

Kenji Sueyoshi is a tenure-track research associate of the Graduate School of Engineering, Osaka Prefecture University (Japan). He received his Ph.D. from Kyoto University in 2008. After staying on as a JSPS fellow at Kyoto University, he was appointed a research associate of Kyoto University in 2009 and, then, moved to Osaka Prefecture University in 2013. His current field of interest includes microscale separation techniques, capillary electrophoresis, and microfluidic devices.

Hideaki Hisamoto is a professor of the Graduate School of Engineering, Osaka Prefecture University (Japan). He received his Ph.D. from Keio University under the guidance of Prof. Koji Suzuki in 1996. Afterward, he stayed at Keio University as a research associate. In 1999, he moved to the University of Tokyo as a lecturer, and he joined Prof. Takehiko Kitamori's group for the development of microscale analytical and synthetic systems using microfabricated devices. In 2003, he was promoted to an associate professor at the Himeji Institute of Technology (currently University of Hyogo) and joined Prof. Shigeru Terabe's and Prof. Fumio Mizutani's groups. In 2007, he moved to Osaka Prefecture University as an associate professor and joined Prof. Toshio Yao's group. In April 2010, he was promoted to full professor. His research interests lie in the development and application of novel analytical methods based on molecular recognition chemistry, chemical sensors, microfluidic devices, and capillary electrophoresis.

Tatsuro Endo is an associate professor of the Graduate School of Engineering, Osaka Prefecture University (Japan). He received his Ph.D. from the Japan Advanced Institute of Science and Technology (JAIST), Biotechnology Laboratory in the Dept. of Biological Science and Biotechnology, in 2006. He was appointed a research associate of Tokyo Institute of Technology in 2006 and, then, moved to Osaka Prefecture University in 2011. His current field of interest includes nanophotonics, biophotonics, and plasmonics.